Catalysis Science & Technology

ROYAL SOCIETY OF CHEMISTRY

PAPER

View Article Online
View Journal | View Issue



Cite this: *Catal. Sci. Technol.*, 2025, 15, 3298

# Enhancing the low-temperature performance of Pt-based three-way catalysts using $CeO_2$(core)@$ZrO_2$(shell) supports†‡

Chih-Han Liu,[a] Junjie Chen, §*[a] Patrick R. Raffaelle,[b] Michael J. Lance,[c] Jacob Concolino,[a] Prateek Khatri,[a] Tala Mon,[a] Todd J. Toops,[c] Alexander A. Shestopalov [b] and Eleni A. Kyriakidou *[a]

Developing robust Pt/$CeO_2$-based three-way catalysts (TWCs) with enhanced oxygen buffering capability and low-temperature activity is highly desirable. In this study, a new TWC family, Pt/(1 – *x*)$CeO_2$(core)@*x*$ZrO_2$(shell) (where *x* = 0–0.5), was prepared and evaluated at degreened (DG) and hydrothermally aged (HTA) states. Incorporation of 0.1 molar concentration of $ZrO_2$ resulted in a decreased temperature that 50% ($T_{50}$) (CO: 167 °C, THCs: 218 °C, NO: 228 °C) and 90% ($T_{90}$) (CO: 207 °C, THCs: 237 °C, NO: 244 °C) conversions achieved over HTA 1.8 wt% Pt/0.9$CeO_2$@0.1$ZrO_2$ compared to the HTA 1.8 wt% Pt/$CeO_2$ sphere (CO: $T_{50,90}$ = 179, 222 °C, THCs: 234, 252 °C, $NO_x$: 240, 260 °C). An enhanced oxygen storage capacity and oxygen release rate were observed over Pt/0.9$CeO_2$@0.1$ZrO_2$ compared to the Pt/$CeO_2$ sphere. Increasing the $ZrO_2$ molar concentration to values greater than 0.2 resulted in increased $T_{50}$s (224, 265 274 °C) and $T_{90}$s (251, 289, 292 °C) for CO, THCs, and $NO_x$, respectively, over 1.8 wt.% Pt/0.5$CeO_2$@0.5$ZrO_2$. Overall, this work highlights the potential of forming a $ZrO_2$ shell on $CeO_2$ spheres as a support for TWC applications.

Received 25th July 2024,
Accepted 11th March 2025

DOI: 10.1039/d4cy00921e

rsc.li/catalysis



## 1. Introduction

Three-way catalysts (TWCs) can simultaneously convert carbon monoxide (CO), hydrocarbons (HCs), and nitrogen oxides ($NO_x$) to less harmful products ($CO_2$, $H_2O$, $N_2$) and they are the key components for the control of stoichiometric spark ignition engine emissions.[1] TWCs are currently highly efficient when the vehicle emission temperature is higher than 350 °C. However, approximately 80% of vehicle emissions are emitted to the atmosphere during the cold start period (first 1–3 min of vehicle operation) when the TWCs are not warm enough.[2] Moreover, the improved engine efficiency of vehicles operating on stoichiometric feed has led to low engine operating temperatures and lower exhaust temperatures. Low exhaust temperatures in gasoline aftertreatment systems necessitate the development of TWCs that are active at low temperatures.[3–5] Specifically, the "150 °C challenge"[6] aimed to achieve 90% conversion of CO, HCs, and nitrogen $NO_x$ at temperatures as low as 150 °C. The most common commercial TWCs utilize platinum group metals (PGMs), such as Pd,[7] Pd/Rh,[8,9] Pt/Rh,[10,11] and Pt/Pd/Rh,[12,13] which can simultaneously convert CO, HCs, and $NO_x$ to $CO_2$, $H_2O$, and $N_2$, respectively, *via* the following reaction routes:[14]

$$CO + \frac{1}{2}O_2 \rightarrow CO_2$$

$$C_xH_{2y} + \left(x + \frac{1}{2}y\right)O_2 \rightarrow xCO_2 + yH_2O$$

$$CO + NO \rightarrow CO_2 + \frac{1}{2}N_2$$

Pt-based TWCs have attracted significant attention due to the lower cost of Pt ($956 per troy ounce; Jan. 2025) compared to Rh ($4675 per troy ounce; Jan. 2025).[15]

The active metals are often dispersed on a support to maximize their active surface area. The rare earth metal

[a] *Department of Chemical and Biological Engineering, University at Buffalo, The State University of New York, Buffalo, NY 14260, USA.*
*E-mail: jchen299@buffalo.edu, elenikyr@buffalo.edu*
[b] *Hajim School of Engineering and Applied Sciences, University of Rochester, Rochester, New York 14627, USA*
[c] *Oak Ridge National Laboratory, Oak Ridge, TN 37831, USA*

† Electronic supplementary information (ESI) available. See DOI: https://doi.org/10.1039/d4cy00921e



§ Current address: SUNCAT Center for Interface Science and Catalysis, Department of Chemical Engineering, Stanford University, Stanford, CA 94305, USA

oxide, ceria ($CeO_2$), is of particular interest in TWCs because Ce exists in two oxidation states ($Ce^{4+}/Ce^{3+}$) under operating conditions.[1] The $Ce^{4+}/Ce^{3+}$ redox couple allows $CeO_2$ to store/release $O_2$ through a redox reaction ($2CeO_2 \leftrightarrow Ce_2O_3 + 0.5\ O_2$)[16,17] under oxygen-rich/deficient conditions, respectively.[18–20] The oxygen storage capacity (OSC) of $CeO_2$ is important in TWCs as it can buffer the oxygen-rich/deficient conditions resulting from the imprecise control of fuel injection in gasoline vehicles, leading to 1% oscillations for an air/fuel ratio of around 14.7 during vehicle operation.[21,22] Oxygen-rich/deficient conditions can significantly impact the efficiency of TWCs to mitigate CO, HCs, and $NO_x$.[12,23,24] Specifically, oxygen can be stored in $CeO_2$ under lean conditions and can be supplied to the oxidation reactions under rich conditions. Zirconium is typically incorporated into $CeO_2$ to increase its lattice oxygen mobility to further improve the TWC performance.[25–27] For example, a more than an order of magnitude increase in OSC (from 25 to 350 $\mu mol_O\ g^{-1}$) was reported by increasing the Ce : Zr molar ratio from 0 ($CeO_2$) to 1 ($Ce_{0.5}Zr_{0.5}O_2$).[25] Moreover, the CO and $NO_x$ catalytic activity over $Pd/CeO_2–ZrO_2–Pr_2O_3$ with various Ce : Zr ratios revealed that a higher OSC (488.4 $mol_O\ g^{-1}$) was responsible for a wider operational window (100% CO conversion at $\lambda \geq 0.925$ and 100% NO conversion at $\lambda \leq 1.075$).[26]

Although $CeO_2$ possesses high OSC, it can suffer from sintering when exposed to elevated temperatures. For instance, TWCs can exposed to 900–950 °C during deceleration fuel cut-offs, scavenging, and disabled fuel enrichment at high engine loads.[28] Polyhedral $CeO_2$, commonly used in catalytic reactions,[29–31] losses the majority of its surface area when exposed to elevated temperatures. Specifically, the surface area of polyhedral $CeO_2$ is decreased from 89 to 21 $m^2\ g^{-1}$ when increasing the calcination temperature from 450 to 600 °C.[32] Therefore, $CeO_2$ supports that can maintain their surface area after exposure to elevated temperatures attract a lot of interest. Several strategies have been adopted to enhance the thermal stability of $CeO_2$. In a study by Chen *et al.*, $CeO_2$ islands were anchored onto the surface of penta-site rich $Al_2O_3$ leading to smaller $CeO_2$ crystalline sizes (~11–17 nm) than the bare $CeO_2$ sample (~22 nm) after hydrothermal aging.[1] Other methods include the incorporation of $ZrO_2$ to the $CeO_2$ lattice to form ceria–zirconia solid solutions.[32] Herein, an approach of coating $CeO_2$ nanospheres with a $ZrO_2$ shell is studied by synthesizing $(1-x)CeO_2@xZrO_2$ ($x$ = 0, 0.1, 0.2, 0.3, 0.5) supports for TWC applications. The TWC activity and hydrothermal stability of $Pt/(1-x)CeO_2@xZrO_2$ catalysts were evaluated using the U.S. DRIVE test protocol.[33] High-resolution transmission electron microscopy (HRTEM), scanning transmission electron microscopy (STEM), and energy dispersive X-ray spectroscopy (EDS) were conducted to reveal the morphology of $(1-x)CeO_2@xZrO_2$. Moreover, CO-pulse chemisorption and CO diffuse reflectance infrared Fourier transform spectroscopy (CO-DRIFTS) were conducted to identify the Pt dispersion. X-ray photoelectron spectroscopy (XPS) was used to determine the Ce oxidation states. Finally, complete oxygen storage capacity (OSCC) and oxygen release rate (ORR) measurements were conducted to elucidate their effect on the TWC performance.

# 2. Experimental

## 2.1. Reagents and materials

Zirconium(IV) butoxide ($Zr(BuO)_4$) solution (80 wt% in 1-butanol, Sigma-Aldrich), anhydrous ethanol (EtOH, 200 proof, Decon), ethylene glycol ($C_2H_6O_2$) (Fisher Scientific, 99.99%), ammonium hydroxide ($NH_4OH$, 28–30 wt% solution of $NH_3$ in water, Sigma-Aldrich), 2,2,4-trimethylpentane ($i$-$C_8H_{18}$) (Sigma Aldrich, 99.8%), and silicon carbide (SiC) (Alfa Aesar, ≥98%) were used as received. A Brij30 solution (100 wt%, Acros Organics, purity 99.79%) was diluted with D.I. water to a 3.8 wt% Brij30 solution prior to usage. Cerium(III) nitrate hexahydrate ($Ce(NO_3)_3{\cdot}6H_2O$) (Sigma Aldrich, 99.999%), zirconium(IV) oxynitrate hydrate ($ZrO(NO_3)_2{\cdot}xH_2O$) (Sigma Aldrich, 99%), and tetraammineplatinum nitrate ($Pt(NH_3)_4(NO_3)_2$) (STREM Chemicals, 99%) were diluted with D.I. water to form 0.1 M, 0.5 M $Ce(NO_3)_3$, 0.1 M $ZrO(NO_3)_2$, and 0.015 M $Pt(NH_3)_4(NO_3)_2$ solutions prior to usage. D.I. water with a resistivity of 18.2 MΩ cm was used for all the syntheses in this study.

## 2.2. Catalyst synthesis

$CeO_2$ spheres were prepared by a hydrothermal synthesis method (Scheme 1).[34] Briefly, $CeO_2$ spheres were synthesized by mixing 5.2 mL of 0.5 M $Ce(NO_3)_3$ solution with 78 mL ethylene glycol and the obtained solution was stirred for 4 h. The mixture was then transferred to an autoclave fitted with a Teflon liner and heated to 180 °C for 8 h, followed by cooling down to room temperature. The obtained mixture was centrifuged at 5000 rpm for 20 min and the solid phase was redispersed in D.I. water and centrifuged three times. The solid phase was subsequently redispersed in anhydrous EtOH and centrifuged three times. The retrieved solid phase was then dried (110 °C/overnight) and calcined (500 °C/2 h) to obtain $CeO_2$ spheres.

$(1-x)CeO_2@xZrO_2$ supports were synthesized using $CeO_2$ spheres (dispersed in anhydrous EtOH). Briefly, $CeO_2$ spheres were dispersed in 39 g anhydrous EtOH, followed by the addition of 0.13 mL of 3.8 wt% Brij 30 solution under constant stirring at room temperature. The solution was stirred for an hour, followed by the addition of 0.132, 0.297, 0.509, and 1.189 mL of 0.1 M $Zr(BuO)_4$, followed by overnight stirring to synthesize $(1-x)CeO_2@xZrO_2$ with $x$ = 0.1, 0.2, 0.3, 0.5, respectively. The solution was centrifuged and redispersed in 50 mL D.I. water. This step was repeated four times. The solution was then aged for 3 days at room temperature. The solid phase was separated, followed by drying (110 °C/overnight) and calcination (500 °C/2 h).

The reference $Ce_{0.9}Zr_{0.1}O_2$ solid solution support was synthesized by co-precipitation as reported previously[32] for an immediate comparison with $0.9CeO_2@0.1ZrO_2$. Briefly, 72

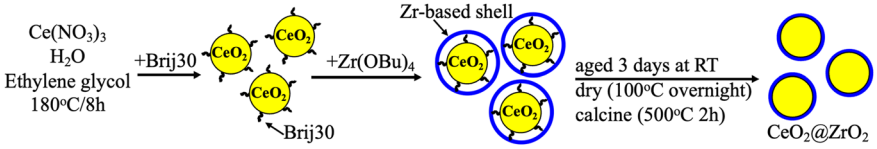


**Scheme 1** Synthesis procedure of $CeO_2$@$ZrO_2$ supports.



mL of 0.1 M $Ce(NO_3)_3$ solution and 8 mL of 0.1 M $ZrO(NO_3)_2$ solution were mixed, resulting in a Ce/Zr precursor solution. This Ce/Zr precursor solution was added dropwise into 48 mL of $NH_4OH$ under stirring. The solution was stirred for 30 min. The formed precipitant was washed with 50 mL D.I. water followed by vacuum filtation. The obtained solids were dried (110 °C/overnight) and calcined (500 °C/2 h).

1.8 wt% Pt was deposited to $(1-x)CeO_2@xZrO_2$ ($x$ = 0.1, 0.2, 0.3, 0.5) and $Ce_{0.9}Zr_{0.1}O_2$ by wet-impregnation. Specifically, 6.3 mL of 0.015 M $Pt(NH_3)_4(NO_3)_2$ solution was added to 1 g of $(1-x)CeO_2@xZrO_2$ and $Ce_{0.9}Zr_{0.1}O_2$ supports. The liquid was evaporated under stirring at room temperature, followed by drying (110 °C/overnight) and calcination (500 °C/2 h).

### 2.3. Material characterization

The Brunauer–Emmett–Teller (BET) surface areas of as-synthesized supports and catalysts were determined by nitrogen physisorption with a Micromeritics Tri-Star II surface area analyzer.

The morphology of $(1-x)CeO_2@xZrO_2$ ($x$ = 0 and 0.3) supports was determined by HRTEM, STEM, and EDS techniques. HRTEM images were obtained at an accelerating voltage of 200 kV using a JEM-2010 equipment. The powdered samples were dispersed in anhydrous EtOH (HRTEM) and isopropyl alcohol (STEM, EDS) followed by ultrasonication. The obtained mixture was then added dropwise onto carbon-coated copper grids (Electron Microscopy Sciences, CF300-CU) followed by drying in air at room temperature. STEM images and EDS elemental maps of individual particles were collected using an FEI Talos F200X.

X-ray diffraction (XRD) patterns of $(1-x)CeO_2@xZrO_2$ ($x$ = 0, 0.1, 0.2, 0.3, 0.5) supports were collected using a Rigaku Ultima IV with a Cu Kα X-ray source. The data were collected from $2\theta$ = 10 to 90° with a step size of 0.02° and scan speed of 2° $min^{-1}$.

CO-pulse chemisorption experiments were conducted using a Micromeritics AutoChem II 2920 equipped with a thermal conductivity detector. An approximately 50 mg sample was loaded in a U-shaped quartz tube reactor. The catalysts were initially oxidized with 20% $O_2$/Ar at 500 °C for 30 min. The catalysts were then cooled down to 250 °C in Ar, followed by purging with Ar for 30 min to remove physisorbed $O_2$. The catalysts were then reduced with 10% $H_2$/Ar for 30 min at 250 °C followed by purging with Ar for another 30 min to remove physisorbed $H_2$. The reactor was immersed in a dry ice–ethanol mixture and cooled to −78 °C under a He flow to prevent CO adsorption on $CeO_2$.[35] CO pulses (10% CO/He, 0.5 $cm^3$) were injected every 5 min until no CO consumption was observed. The total flow rate for the CO-pulse chemisorption experiment was maintained at 50 sccm ($cm^3$ $min^{-1}$ (STP)). The Pt particle size was calculated assuming all particles were equally sized hemispheres and a stoichiometry of CO/Pt = 1 was assumed.[36]

CO-DRIFTS experiments were performed as reported previously[37] using a Nicolet iS50 FTIR spectrometer (Thermo Fisher) equipped with a high temperature reaction chamber (Harrick Praying Mantis). An approximately 25 mg sample was loaded in a sample holder and it was initially pretreated in Ar at 200 °C for 30 min. The sample was then cooled down to 25 °C in Ar, where background spectra were collected at a resolution of 4 $cm^{-1}$ and 32 scans. Samples were then exposed to 1% CO/Ar for 30 min, followed by purging with Ar for another 30 min to remove gas phase CO. The total flow rate for the CO-DRIFTS experiments was 100 sccm.

The OSCC and ORR were measured using the low-temperature TWC test protocol defined by U.S. DRIVE in a customized reactor setup described in section 2.4.[33] OSCC measurements on ~25 mg of degreened catalyst were performed isothermally from 550 °C to 350 °C to 150 °C. The catalysts were initially exposed to 1.5% $O_2$/Ar for 10 min, followed by switching to 0.2% CO/Ar for another 10 min. The switch from one gas stream to another was facilitated with an automated four-way valve for a smoother transition. Before exposure to $O_2$ at each steady-state temperature, the catalyst surface was purged with Ar for 30 min. The OSCC was calculated by integrating the CO consumption from 0 to 10 min and the ORR was calculated from the slope of the CO concentration *vs.* time plot between 6 and 9 s after 0.2% CO/Ar was introduced to the feed stream. CO ($m/z$ = 29) and Ar ($m/z$ = 40) signals were recorded with a Pfeiffer Omnistar GSD 320 mass spectrometer with a 200 ms interval.

XPS spectra were recorded on a Kratos Axis Ultra XPS spectrometer equipped with an Al Kα (1486.6 eV) X-ray source at 200 W power and a pressure of $3.0 \times 10^{-8}$ mbar. Survey scans were obtained between 0 and 1200 eV with a step size of 1 eV, a dwell time of 200 ms, and a pass energy of 140 eV averaged over 5 scans. Core-level region scans for Ce 3d, Zr 3d, C 1s, and O 1s were obtained at the corresponding binding energy ranges with a step size of 0.1 eV, an average dwell time of 260 ms, and a pass energy of 20 eV averaged over 5 scans. Data processing was performed using CasaXPS software employing Shirley-routine background subtraction and instrument-specific atomic sensitivity factors.

 

### 2.4. Catalyst evaluation

Catalyst evaluation was performed in a customized U-shaped quartz reactor, as reported previously.[38] Briefly, 100 mg of catalyst powder diluted with 200 mg SiC was placed in the reactor tube stabilized by two loosely packed quartz wool plugs. The reactor was then placed in a cylindrical furnace surrounded by quartz wool to eliminate heat gradients. A K-type thermocouple was inserted into the top quartz wool plug in the U-shaped reactor to record the inlet gas temperature. Another K-type thermocouple was attached outside the reactor at the same height as the inlet temperature thermocouple to allow the PID temperature controller to control the furnace temperature. The gases used to simulate the TWC performance were purchased from Airgas and were the following: 99.999% $CO_2$, 99.999% $O_2$ (UHP), 10.01% $H_2$/Ar, 10.1% CO/Ar, 1% NO/Ar, 5% $C_2H_4$/Ar, 5% $C_3H_6$/Ar, 1% $C_3H_8$/Ar, and 99.999% Ar (UHP). All gases were regulated by a set of MKS mass flow controllers. Liquid *i*-$C_8H_{18}$ was placed in a bubbler immersed in a controlled temperature (0 °C) water bath and gas phase *i*-$C_8H_{18}$ was carried by Ar to the reactor. The Clausius–Clapeyron equation and the vapor pressure of *i*-$C_8H_{18}$ (1.78 kPa at 0 °C)[39] were used to calculate the Ar flow required to carry *i*-$C_8H_{18}$ from the bubbler to the reactor. Water was supplied to the reactor (0.027 mL $min^{-1}$) by a D-series pump (Teledyne Isco) and steam was generated in a tube furnace set at 200 °C that was carried by Ar to the reactor. The catalytic performance experiments were conducted from 100 to 500 °C at a heating rate of 2 °C $min^{-1}$. The temperature was recorded every second using a LabView program. The total flow rate was maintained to 333 sccm, corresponding to a gas hourly space velocity of 142 500 $h^{-1}$. The reactor outlet gas was diluted with 1332 sccm Ar and analyzed using an MKS MultiGas 2030 FTIR gas analyzer operating at 191 °C. The reactor gas lines were heated at 170 °C to avoid water condensation.

Catalysts were evaluated after degreening (DG) and redox hydrothermal aging (HTA). Degreening of the catalysts was conducted at 700 °C for 4 h under 10% $H_2O$, 10% $CO_2$, Ar balance. Redox HTA was conducted at 800 °C for 10 h at a switching frequency of 0.1 Hz between a lean (5% $O_2$, 10% $H_2O$, 10% $CO_2$, Ar balance) and a rich (3% CO, 1% $H_2$, 10% $H_2O$, 10% $CO_2$, Ar balance) gas stream. Prior to evaluating the DG and HTA catalysts, the catalysts were pretreated at 600 °C (10% $H_2O$, 13% $CO_2$, Ar balance) for 20 min. Simulated TWC oxidation experiments were performed using the low temperature oxidation catalyst test protocol stoichiometric gasoline direct injection (S-GDI) gas composition defined by U.S. DRIVE[33] (13% $CO_2$, 10% $H_2O$, stoichiometric $O_2$, 1670 ppm $H_2$, 5000 ppm CO, 1000 ppm NO, 700 ppm $C_2H_4$, 1000 ppm $C_3H_6$, 300 ppm $C_3H_8$, 1000 ppm *i*-$C_8H_{18}$, hydrocarbons in $C_1$ basis, Ar balance).

## 3. Results and discussion

### 3.1. Surface characterization

The BET surface areas and $N_2$ adsorption/desorption isotherms of $(1-x)CeO_2@xZrO_2$ (where $x$ = 0, 0.1, 0.2, 0.3, and 0.5) and $Ce_{0.9}Zr_{0.1}O_2$ solid solution supports are summarized in Table S1 and Fig. S1,† respectively. All $(1-x)$ $CeO_2@xZrO_2$ supports have surface areas of 69.3–95 $m^2$ $g^{-1}$ and type II isotherms, characteristic of non-porous or macroporous materials.[40] The solid solution $Ce_{0.9}Zr_{0.1}O_2$ has a surface area of 77.2 $m^2$ $g^{-1}$ and a type IV isotherm, characteristic of mesoporous materials.

The morphology of synthesized $CeO_2$ is spherical (Fig. S2†) with a uniform diameter of ~160 nm. Fig. 1(a, b and d) show the HRTEM image and EDS maps of the $0.7CeO_2@0.3ZrO_2$ support. The EDS elemental maps of Ce and Zr suggest that the $ZrO_2$ overlayer covers the surface of $CeO_2$ uniformly. Fig. 1(c) shows that $ZrO_2$ is enriched in the shell layer of $0.7CeO_2@0.3ZrO_2$, while the Ce signal is more dominant in the core and decreases when approaching the shell, suggesting that a core@shell structure was prepared. However, an uneven $ZrO_2$ coating was formed (Fig. S3†) when the Zr molar concentration increased from 0.3 ($0.7CeO_2@0.3ZrO_2$) to 0.5 ($0.5CeO_2@0.5ZrO_2$), attributed to excess $ZrO_2$ that cannot be coated evenly.

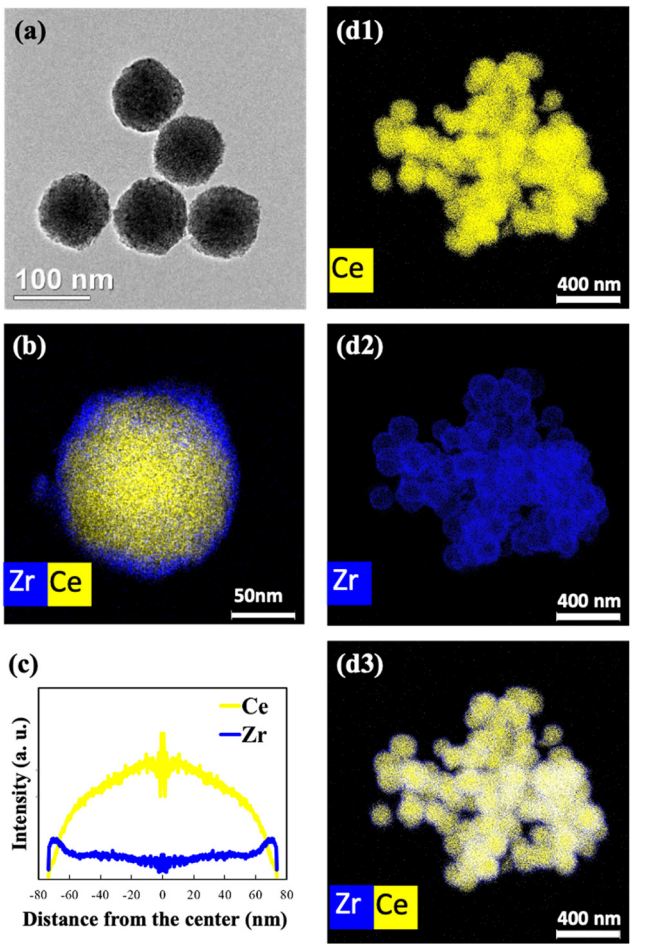


Fig. 1 (a) HRTEM image, (b and d) EDS elemental maps of Ce and Zr of the $0.7CeO_2@0.3ZrO_2$ support and (c) Ce and Zr elemental distributions obtained by converting the brightness in intensity from the EDS elemental map in (b).

XRD spectra of the (1 − $x$)$CeO_2$@$xZrO_2$ supports (Fig. 2) show that $CeO_2$ spheres possess peaks at 2$\theta$ of 28.5° and 33.1° that correspond to the (111) and (200) planes of cubic $CeO_2$, respectively.[41] Increasing the Zr molar concentration to values ≥0.2 led to the appearance of additional peaks at 30.2 and 35.2°, which correspond to the (111) and (200) planes of tetragonal $ZrO_2$, respectively.[42,43]

The average Pt particle size and dispersion of 1.8 wt% Pt/(1 − $x$)$CeO_2$@$xZrO_2$ were obtained by CO-pulse chemisorption (Fig. 3). The Pt/$CeO_2$ sphere showed an average Pt particle size of 7.7 nm, corresponding to a Pt dispersion of 13.5%. Similar average Pt particle sizes and dispersions were observed over Pt/(1 − $x$)$CeO_2$@$xZrO_2$ with $x \leq 0.2$. Specifically, the average Pt particle size of Pt/0.9$CeO_2$@0.1$ZrO_2$ and Pt/0.8$CeO_2$@0.2$ZrO_2$ was 6.8 nm (Pt dispersion: 15.4%) and 7.2 nm (Pt dispersion: 15.7%), respectively. The similar Pt particle size and dispersion observed at low Zr molar concentrations suggest the existence of strong metal–support interactions between Pt and $CeO_2$.[44] An increase in Zr molar concentration to 0.3 and 0.5 in Pt/(1 − $x$)$CeO_2$@$xZrO_2$ led to an increase in the average Pt particle size to 9.9 nm (Pt dispersion: 11.4%) and 14.3 nm (Pt dispersion: 7.9%), respectively.

CO-DRIFTS experiments conducted over Pt/(1 − $x$)$CeO_2$@$xZrO_2$ catalysts (Fig. 4) showed that Pt/(1 − $x$)$CeO_2$@$xZrO_2$ contains two types of Pt species. The high wavenumber peak (2097 $cm^{-1}$) is attributed to CO adsorbed on ionic $Pt^{2+}$ strongly interacting with $CeO_2$.[45,46] The low wavenumber peak (2087 $cm^{-1}$) is attributed to CO adsorbed on $Pt^0$ particles.[47,48] The 2097 $cm^{-1}$ and 2087 $cm^{-1}$ peaks are more pronounced at low ($x \leq 0.1$) and high ($x > 0.1$) Zr molar concentrations, respectively. This observation suggests that increasing the molar concentration of Zr can hinder the occurrence of $Pt^{2+}$ species that can strongly interact with $CeO_2$. Instead, $Pt^0$ particles are formed, consistent with the CO-pulse chemisorption results that show a decreased Pt dispersion with increasing Zr molar concentration.

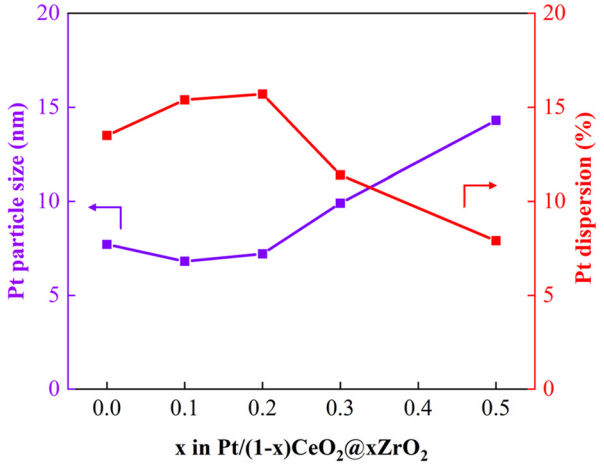


Fig. 3 Average Pt particle size and dispersion of 1.8 wt% Pt/(1 − $x$)$CeO_2$@$xZrO_2$ catalysts obtained by CO-pulse chemisorption.

The XPS survey of 0.9$CeO_2$@0.1$ZrO_2$ (Fig. S4†) shows the presence of 16.6 atomic% of Zr, suggesting the successful deposition of $ZrO_2$ on the surface of 0.9$CeO_2$@0.1$ZrO_2$. The XPS results for Ce 3d of the $CeO_2$ spheres and 0.9$CeO_2$@0.1$ZrO_2$ supports are shown in Fig. 5. The peaks labeled Vo, V′, $u_0$, and u′ correspond to $Ce^{3+}$ and peaks labeled u, u″, u‴, v, v″, and v‴ correspond to $Ce^{4+}$.[49] The peak area that belongs to $Ce^{3+}$ is 13.0% and 17.2 % for $CeO_2$ spheres and 0.9$CeO_2$@0.1$ZrO_2$, respectively, suggesting that Zr incorporation leads to a higher $Ce^{3+}/Ce^{4+}$ ratio. It was reported that oxygen vacancies from nano-sized $CeO_2$ are associated with the presence of $Ce^{3+}$ on the surface resulting in a higher $Ce^{3+}/Ce^{4+}$ ratio compared to bulk $CeO_2$.[50] Therefore, the increase of $Ce^{3+}/Ce^{4+}$ ratio in 0.9$CeO_2$@0.1$ZrO_2$ may result in a higher oxygen storage capacity and oxygen release rate (discussed in section 3.2).

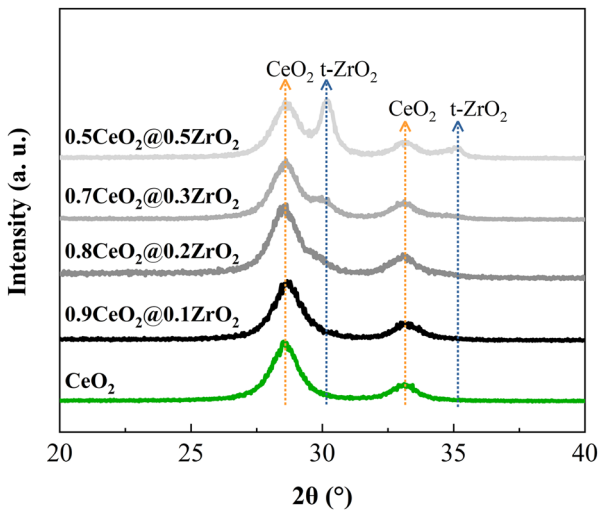


Fig. 2 XRD patterns of (1 − $x$)$CeO_2$@$xZrO_2$ ($x$ = 0, 0.1, 0.2, 0.3, 0.5) supports (t: tetragonal).

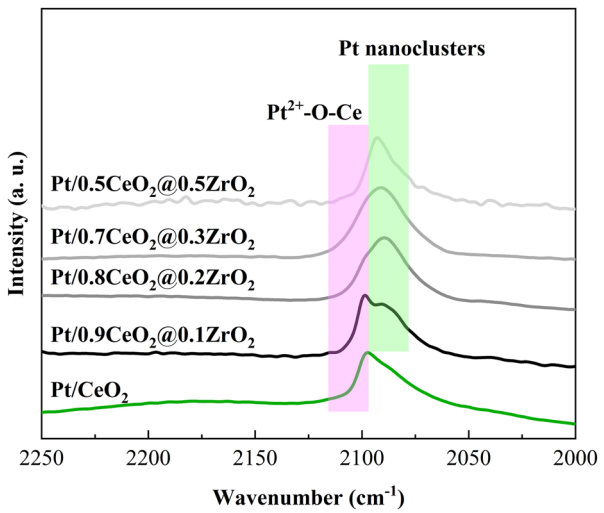


Fig. 4 CO-DRIFTS over fresh 1.8 wt% Pt/(1 − $x$)$CeO_2$@$xZrO_2$ ($x$ = 0, 0.1, 0.2, 0.3, 0.5) catalysts.

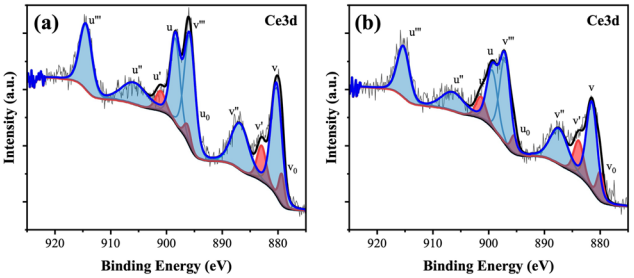


Fig. 5 XPS results for Ce 3d of (a) $CeO_2$ and (b) $0.9CeO_2$@$0.1ZrO_2$.

### 3.2. TWC performance

The temperatures that 50% and 90% CO, total HCs (THCs) and $NO_x$ conversions achieved ($T_{50}$ and $T_{90}$, respectively) over Pt/(1 ~ $x$)$CeO_2$@$xZrO_2$ (DG) catalysts are summarized in the bar chart shown in Fig. 6 and the light off curves shown in Fig. S5.† $T_{90}$s for CO/THCs/$NO_x$ were achieved at 207 °C/244 °C/256 °C over Pt/$CeO_2$ spheres (DG), respectively. The performance improved with the incorporation of 0.1 molar concentration of Zr. Specifically, Pt/$0.9CeO_2$@$0.1ZrO_2$ (DG) achieved $T_{90}$s for CO (188 °C), THCs (229 °C), and $NO_x$ (240 °C) at a lower temperature compared to Pt/$CeO_2$ spheres (DG). Further, Pt/$0.8CeO_2$@$0.2ZrO_2$ (DG) showed a slightly improved performance compared to Pt/$0.9CeO_2$@$0.1ZrO_2$ (DG) with $T_{90}$s achieved at 185 °C, 223 °C, and 234 °C for CO, THCs, and $NO_x$, respectively. However, a further increase in Zr molar concentration to ≥0.3 led to a decrease in the catalytic performance with a shift in $T_{90}$s to higher temperatures. For instance, the $T_{90}$s achieved over Pt/$0.7CeO_2$@$0.3ZrO_2$ (DG) and Pt/$0.5CeO_2$@$0.5ZrO_2$ (DG) were 206 °C/245 °C/254 °C and 216 °C/255 °C/268 °C for CO/THCs/$NO_x$, respectively. The decreased performance of the catalysts with Zr loadings ≥0.3 can be attributed to sintering of Pt particles on crystallized $ZrO_2$. Furthermore, the activity of 1.8 wt% Pt/$Ce_{0.9}Zr_{0.1}O_2$ (DG) was compared to 1.8 wt% Pt/$0.9CeO_2$@$0.1ZrO_2$ (DG) (Fig. S6a†). The results indicate that Pt/$0.9CeO_2$@$0.1ZrO_2$ (DG) outperformed Pt/$Ce_{0.9}Zr_{0.1}O_2$ (DG), with the latter achieving $T_{90}$s of CO/THCs/$NO_x$ at 205 °C/248 °C/260 °C, respectively.

The oxygen storage/release properties of the catalyst are crucial in near stoichiometric TWC reactions. Therefore, the OSCC and ORR of Pt/(1 − $x$)$CeO_2$@$xZrO_2$ (DG) were measured and correlated with the catalytic performance results (Fig. 7 and S7†). The Pt/$CeO_2$ sphere had an OSCC and ORR of 155 μmol $g^{-1}$ and 4.7 μmol $g^{-1}$ $s^{-1}$, respectively. The OSCC and ORR were improved when a small amount of $ZrO_2$ ($x$ = 0.1, 0.2) was deposited on $CeO_2$ spheres. Specifically, Pt/$0.9CeO_2$@$0.1ZrO_2$ and Pt/$0.8CeO_2$@$0.2ZrO_2$ had a greater OSCC (259 and 246 μmol $g^{-1}$, respectively) and ORR (5.2 and 5.1 μmol $g^{-1}$ $s^{-1}$, respectively) compared to Pt/$CeO_2$ spheres. However, further addition of Zr (molar concentrations >0.2) decreased the OSCC and ORR. Specifically, the OSCC decreased to 211 and 185 μmol $g^{-1}$ and the ORR decreased to 4.6 and 4.1 μmol $g^{-1}$ $s^{-1}$ for Zr molar concentrations of 0.3 and 0.5, respectively. Fig. 7 shows that an increase in OSCC and ORR was accompanied by a decrease in $T_{50}$s and *vice versa*, implying that optimization of the OSCC and ORR of Pt/(1 − $x$)$CeO_2$@$xZrO_2$ (DG) by varying the Zr molar concentrations can tune the TWC performance. The ORR of bare supports was measured at three different temperatures (150, 350, and 550 °C). $0.7CeO_2$@$0.3ZrO_2$ showed an enhanced ORR compared to $CeO_2$ spheres at 150 °C and a similar ORR compared to $CeO_2$ spheres at 350 and 550 °C (Fig. S8†). Moreover, $0.7CeO_2$@$0.3ZrO_2$ and the $Ce_{0.7}Zr_{0.3}O_2$ solid solution showed a similar ORR at 150 °C, while $0.7CeO_2$@$0.3ZrO_2$ showed a greater ORR than the $Ce_{0.7}Zr_{0.3}O_2$ solid solution at 350 and 550 °C.

The hydrothermal stability of Pt/(1 − $x$)$CeO_2$@$xZrO_2$ was assessed after redox HTA was conducted, followed by a TWC performance evaluation. The evaluation results of Pt/(1 − $x$)$CeO_2$@$xZrO_2$ (HTA) catalysts are summarized in Fig. 8 and Fig. S9.† All catalysts showed higher $T_{50,90}$s compared to their DG states (Fig. 6), suggesting that the catalysts deactivate after redox HTA. For example, the Pt/$CeO_2$ sphere (HTA) reached $T_{90}$s for CO/THCs/$NO_x$ at 222 °C/252 °C/258 °C, which are 15 °C/8 °C/3 °C higher than the $T_{90}$s achieved over Pt/$CeO_2$ sphere (DG), respectively. Deposition of the Zr shell with a Zr molar concentration <0.2 alleviated the

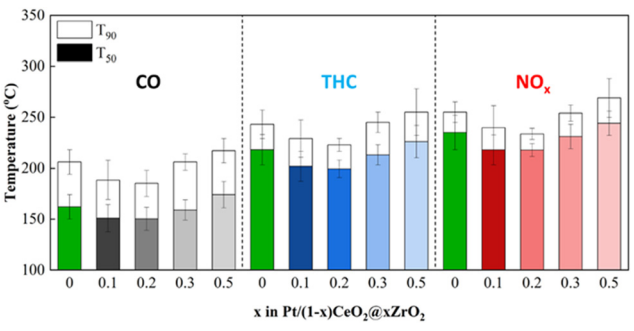


Fig. 6 Comparison of $T_{50,90}$s of CO, THCs and $NO_x$ over DG 1.8 wt% Pt/(1 ~ $x$)$CeO_2$@$xZrO_2$ ($x$ = 0, 0.1, 0.2, 0.3, 0.5) catalysts; each bar represents the average $T_{50,90}$s of three different batches of the catalyst and the error bars represent the standard deviation of the $T_{50,90}$s.

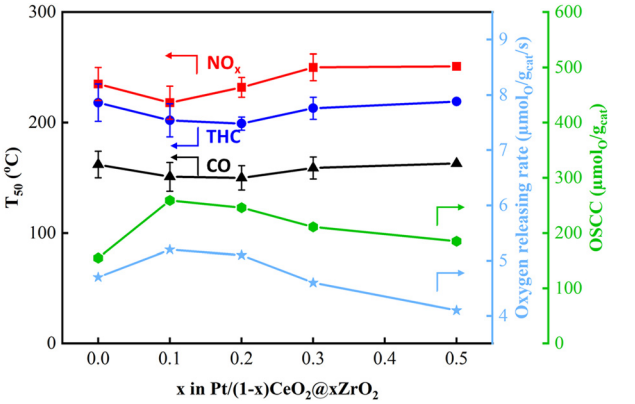


Fig. 7 $T_{50}$s of CO, THCs, $NO_x$ (left) and OSCC and ORR (right) of 1.8 wt% Pt/(1 − $x$)$CeO_2$@$xZrO_2$ (DG) catalysts.

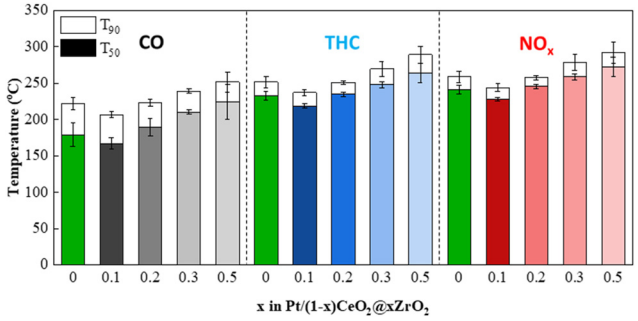


Fig. 8 Comparison of $T_{50,90}$s of CO, THCs and $NO_x$ for 1.8 wt% Pt/(1 − $x$)$CeO_2$@$xZrO_2$ (HTA) ($x$ = 0, 0.1, 0.2, 0.3, 0.5) catalysts; each bar represents the average $T_{50,90}$s of the three different batches of the catalyst and the error bars represent the standard deviation of the $T_{50,90}$s.

deactivation caused by redox HTA and improved the catalytic performance compared to the $Pt/CeO_2$ sphere (HTA). For instance, $Pt/0.9CeO_2@0.1ZrO_2$ (HTA) achieved lower $T_{90}$s for CO (207 °C), THCs (237 °C), and $NO_x$ (244 °C) compared to $Pt/CeO_2$ (HTA) with $T_{90}$s for CO/THCs/$NO_x$ achieved at 222 °C/252 °C/258 °C, respectively. Moreover, $Pt/0.9CeO_2@0.1ZrO_2$ (HTA) outperformed $Pt/0.8CeO_2@0.2ZrO_2$ (HTA) (CO/THCs/$NO_x$ $T_{90}$s achieved at 223 °C/251 °C/258 °C, respectively). A further increase in Zr molar concentrations to 0.3 and 0.5 led to higher $T_{90}$s for $Pt/0.7CeO_2@0.3ZrO_2$ (HTA) (239 °C (CO)/270 °C (THCs)/279 °C ($NO_x$)) and $Pt/0.5CeO_2@0.5ZrO_2$ (HTA) (252 °C (CO)/289 °C (THCs)/292 °C ($NO_x$)). Finally, $Pt/0.9CeO_2@0.1ZrO_2$ (HTA) outperformed the $Pt/Ce_{0.9}Zr_{0.1}O_2$ (HTA) (Fig. S6†) solid solution catalyst, with the latter achieving $T_{90}$s at 220 °C/262 °C/263 °C for CO/THCs/$NO_x$, respectively. This behavior indicates the advantage of the formation of the (1 − $x$)$CeO_2$@$xZrO_2$ structured support compared to the bare $CeO_2$ support. TEM images of redox HTA $Pt/0.9CeO_2@0.1ZrO_2$ (Fig. S10†) showed mild sintering of the spherical support, while no large Pt nanoparticles were identified, which is consistent with the CO-DRIFTS results (Fig. 4). $Pt/CeO_2$ and $Pt/0.9CeO_2@0.1ZrO_2$ showed the lowest $\Delta T_{50}$s (= $T_{50,HTA}$ − $T_{50,DG}$) (Fig. S11†), suggesting the least deactivation after redox HTA compared to the rest of the studied catalysts. The $\Delta T_{50}$s increased when the Zr molar concentration increased to values ≥0.2, indicating that a thick $ZrO_2$ coating layer does not favor stability.

## 4. Conclusions

A simulated S-GDI gas mixture was used for the TWC evaluation of a series of Pt/(1 − $x$)$CeO_2$@$xZrO_2$ catalysts. $Pt/CeO_2$ spheres (DG) achieved $T_{90}$s at 207, 244, and 256 °C for CO, THCs, and $NO_x$, respectively. However, deactivation was observed after HTA with the $T_{90}$s of the $Pt/CeO_2$ sphere (HTA) increased to 222, 252, and 258 °C for CO, THCs, and $NO_x$, respectively. With the incorporation of 0.1 molar concentration of Zr, $Pt/0.9CeO_2@0.1ZrO_2$ showed the most promising performance considering both DG and HTA evaluation results by achieving the lowest $T_{90}$s for CO, THCs, and $NO_x$ at 207, 237 and 244 °C (HTA), respectively, compared to all studied Pt/(1 − $x$)$CeO_2$@$xZrO_2$ catalysts. Tuning the Zr molar concentration and thus the Ce : Zr molar ratio of the Pt/(1 − $x$)$CeO_2$@$xZrO_2$ TWCs affected their low temperature catalytic activity by altering their OSCC and ORR. Specifically, improved OSCC (259 μmol $g^{-1}$) and ORR (5.2 μmol $g^{-1}$ $s^{-1}$) values were observed over $Pt/0.9CeO_2@0.1ZrO_2$ (DG), while increasing the Zr molar concentration further led to a decrease in OSCC and ORR. Furthermore, sintering of Pt can be minimized (average Pt particle size of 6.8 nm) over $Pt/0.9CeO_2@0.1ZrO_2$ compared to an excess amount of zirconium ($x$ > 0.2), which contains thick $ZrO_2$ shell that interacts weakly with Pt. Overall, this work highlights the potential of Pt-only catalysts supported on (1 − $x$)$CeO_2$@$xZrO_2$ supports as TWCs and reveals that an improved TWC performance can be achieved by incorporating moderate amounts of zirconium (Zr molar concentration = 0.1).

## Data availability

The data supporting this article have been included as part of the ESI.† Any additional data are available from the corresponding author upon request.

## Conflicts of interest

There are no conflicts to declare.

## Acknowledgements

This work was partially supported by start-up funding from the Department of Chemical and Biological Engineering, University at Buffalo (UB), The State University of New York (SUNY). A portion of this research was sponsored by the U. S. Department of Energy's Vehicle Technology Office, with particular thanks to Gurpreet Singh, Siddiq Khan, and Nicholas Hansford of the Offroad, Rail, Marine and Aviation (ORMA). Additionally, the FEI Talos F200X STEM was provided by the Department of Energy, Office of Nuclear Energy, Fuel Cycle R&D Program and the Nuclear Science User Facilities.

## References

1 J. Chen, C.-H. Liu, H. N. Pham, T. J. Toops, A. K. Datye and E. A. Kyriakidou, Designing ultrastable Pt/CeO2-Al2O3 nanosheet catalysts for three-way catalysts applications, *Chem. Eng. J.*, 2023, **477**, 147086.
2 M. Weilenmann, J.-Y. Favez and R. Alvarez, Cold-start emissions of modern passenger cars at different low ambient temperatures and their evolution over vehicle legislation categories, *Atmos. Environ.*, 2009, **43**(15), 2419–2429.

 

3 J. Lee, J. R. Theis and E. A. Kyriakidou, Vehicle emissions trapping materials: Successes, challenges, and the path forward, *Appl. Catal., B*, 2019, **243**, 397–414, DOI: **10.1016/j.apcatb.2018.10.069**.

4 A. P. Wong, E. A. Kyriakidou, T. J. Toops and J. R. Regalbuto, The catalytic behavior of precisely synthesized Pt–Pd bimetallic catalysts for use as diesel oxidation catalysts, *Catal. Today*, 2016, **267**, 145–156.

5 E. Kyriakidou, T. J. Toops, J.-S. Choi, M. J. Lance and J. E. Parks II Exhaust treatment catalysts with enhanced hydrothermal stability and low-temperature activity, *US Pat.*, 1042137 B2 (October 1, 2019).

6 M. Zammit, C. L. DiMaggio, C. H. Kim, C. Lambert, G. G. Muntean, C. H. Peden, J. E. Parks and K. Howden, *Future automotive aftertreatment solutions: The 150 C challenge workshop report (US Drive Workshop)*, 2012, **https://www.pnnl.gov/main/publications/external/technical_Reports/PNNL-22815.pdf**.

7 S. B. Kang, J. B. Lim, D. Jo, I.-S. Nam, B. K. Cho, S. B. Hong, C. H. Kim and S. H. Oh, Ostwald-ripening sintering kinetics of Pd-based three-way catalyst: Importance of initial particle size of Pd, *Chem. Eng. J.*, 2017, **316**, 631–644.

8 C. Wang, J. Tan, G. Harle, H. Gong, W. Xia, T. Zheng, D. Yang, Y. Ge and Y. Zhao, Ammonia formation over Pd/Rh three-way catalysts during lean-to-rich fluctuations: The Effect of the catalyst aging, exhaust temperature, lambda, and duration in rich conditions, *Environ. Sci. Technol.*, 2019, **53**(21), 12621–12628.

9 A. A. Vedyagin, R. M. Kenzhin, M. Y. Tashlanov, E. A. Alikin, V. O. Stoyanovskii, P. E. Plyusnin, Y. V. Shubin, I. V. Mishakov, M. Y. Smirnov and A. V. Kalinkin, Effect of La addition on the performance of three-way catalysts containing palladium and rhodium, *Top. Catal.*, 2020, **63**, 152–165.

10 J. A. Anderson, R. A. Daley, S. Y. Christou and A. M. Efstathiou, Regeneration of thermally aged Pt-Rh/CexZr1−xO2-Al2O3 model three-way catalysts by oxychlorination treatments, *Appl. Catal., B*, 2006, **64**(3–4), 189–200.

11 J. G. Nunan, H. J. Robota, M. J. Cohn and S. A. Bradley, Physicochemical properties of Ce-containing three-way catalysts and the effect of Ce on catalyst activity, *J. Catal.*, 1992, **133**(2), 309–324.

12 J. Wang, H. Chen, Z. Hu, M. Yao and Y. Li, A review on the Pd-based three-way catalyst, *Catal. Rev.: Sci. Eng.*, 2015, **57**(1), 79–144.

13 V. V. Eskina, O. A. Dalnova, D. G. Filatova, V. B. Baranovskaya and Y. A. Karpov, Direct precise determination of Pd, Pt and Rh in spent automobile catalysts solution by high-resolution continuum source graphite furnace atomic absorption spectrometry, *Spectrochim. Acta, Part B*, 2020, **165**, 105784.

14 I. Mejía-Centeno, A. Martínez-Hernández and G. A. Fuentes, Effect of low-sulfur fuels upon NH3 and N2O emission during operation of commercial three-way catalytic converters, *Top. Catal.*, 2007, **42**(1), 381–385.

15 *Metals Daily*, **https://www.metalsdaily.com/accessed**.

16 Y. Malyukin, P. Maksimchuk, V. Seminko, E. Okrushko and N. Spivak, Limitations of self-regenerative antioxidant ability of nanoceria imposed by oxygen diffusion, *J. Phys. Chem. C*, 2018, **122**(28), 16406–16411.

17 L. Sun, W. Xiao, X. Hao, Q. Meng and M. Zhou, A first-principles study on the structural, thermal and electronic properties of cerium oxides by using different functionals, *Electron. Struct.*, 2018, **1**(1), 015003.

18 P. Li, X. Chen, Y. Li and J. W. Schwank, A review on oxygen storage capacity of $CeO_2$-based materials: Influence factors, measurement techniques, and applications in reactions related to catalytic automotive emissions control, *Catal. Today*, 2019, **327**, 90–115.

19 F. Dong, T. Tanabe, N. Takahashi and H. Shinjoh, Investigation of the effective oxygen storage and release performances on the Pt/$CeO_2$-$ZrO_2$ catalysts by breakthrough method, *Catal. Today*, 2019, **332**, 259–266.

20 C. Paun, O. V. Safonova, J. Szlachetko, P. M. Abdala, M. Nachtegaal, J. Sa, E. Kleymenov, A. Cervellino, F. Krumeich and J. A. van Bokhoven, Polyhedral $CeO_2$ nanoparticles: size-dependent geometrical and electronic structure, *J. Phys. Chem. C*, 2012, **116**(13), 7312–7317.

21 M. V. Twigg, Roles of catalytic oxidation in control of vehicle exhaust emissions, *Catal. Today*, 2006, **117**(4), 407–418.

22 T. Suzuki and M. Ichiyanagi, Robust control design for air-fuel ratio fluctuation of gasoline engine (1st report: Development of feed-forward controller with heat transfer model at intake), *Journal of Japan Society for Design Engineering*, 2018, **53**(5), 377–390.

23 J. A. Cook, I. V. Kolmanovsky, D. McNamara, E. C. Nelson and K. V. Prasad, Control, computing and communications: technologies for the twenty-first century model T, *Proc. IEEE*, 2007, **95**(2), 334–355.

24 O. Barbarisi, A. Gaeta and L. Glielmo, An extended kalman observer for the in-cylinder air mass flow estimation, in *Proceedings of MECA02 International Workshop on Diagnostics in Automotive Engines and Vehicles*, Fisciano SA, Italy, 2002.

25 Q. Dong, S. Yin, C. Guo and T. Sato, Aluminum-doped ceria-zirconia solid solutions with enhanced thermal stability and high oxygen storage capacity, *Nanoscale Res. Lett.*, 2012, **7**(1), 1–5.

26 X. Yang, L. Yang, S. Lin and R. Zhou, Investigation on properties of Pd/$CeO_2$–$ZrO_2$–$Pr_2O_3$ catalysts with different Ce/Zr molar ratios and its application for automotive emission control, *J. Hazard. Mater.*, 2015, **285**, 182–189.

27 R. Wang, L. Lan, M.-C. Gong and Y.-Q. Chen, Catalytic Combustion of Gasoline Particulate Soot over $CeO_2$-$ZrO_2$ Catalysts, *Acta Phys. Chim. Sin.*, 2016, **32**(7), 1747–1757.

28 J. Schoenhaber, J. M. Richter, J. Despres, M. Schmidt, S. Spiess and M. Roesch, *Advanced TWC Technology to Cover Future Emission Legislations*, SAE Tech. Pap., 2015.

29 C. Larese, M. L. Granados, F. C. Galisteo, R. Mariscal and J. Fierro, TWC deactivation by lead: a study of the Rh/$CeO_2$ system, *Appl. Catal., B*, 2006, **62**(1–2), 132–143.

30 L. S. Kibis, D. A. Svintsitskiy, E. A. Derevyannikova, T. Y. Kardash, E. M. Slavinskaya, O. A. Stonkus, V. A. Svetlichnyi

and A. I. Boronin, From highly dispersed $Rh^{3+}$ to nanoclusters and nanoparticles: Probing the low-temperature NO+CO activity of Rh-doped $CeO_2$ catalysts, *Appl. Surf. Sci.*, 2019, **493**, 1055–1066.

31 M. M. Natile and A. Glisenti, Nanostructured $CeO_2$ powders by XPS, *Surf. Sci. Spectra*, 2006, **13**(1), 17–30.

32 J. Chen, B. D. Carlson, T. J. Toops, Z. Li, M. J. Lance, S. Karakalos, J.-S. Choi and E. Kyriakidou, Methane combustion over $Ni/Ce_xZr_{1-x}O_2$ catalysts: impact of ceria/zirconia ratio, *ChemCatChem*, 2020, **12**(21), 5558–5568.

33 K. G. Rappé, C. DiMaggio, J. A. Pihl, J. R. Theis, S. H. Oh, G. B. Fisher, J. Parks, V. G. Easterling, M. Yang and M. L. Stewart, Aftertreatment Protocols for Catalyst Characterization and Performance Evaluation: Low-Temperature Oxidation, Storage, Three-Way, and $NH_3$-SCR Catalyst Test Protocols, *Emiss. Control Sci. Technol.*, 2019, **5**(2), 183–214.

34 Q. Fang and X. Liang, $CeO_2$–$Al_2O_3$, $CeO_2$–$SiO_2$, $CeO_2$–$TiO_2$ core-shell spheres: formation mechanisms and UV absorption, *RSC Adv.*, 2012, **2**(12), 5370–5375.

35 M. Li, J. Deng, X. Yin, W. Wang, Y. Zhao, H. Xu, J. Wang and Y. Chen, Effect of lauric acid on the grain growth of $CeO_2$-$ZrO_2$-$Y_2O_3$-$La_2O_3$ in different periods, *J. Alloys Compd.*, 2022, **894**, 162301.

36 H. Nassiri, K. E. Lee, Y. Hu, R. E. Hayes, R. W. Scott and N. Semagina, Platinum Inhibits Low-Temperature Dry Lean Methane Combustion through Palladium Reduction in Pd–Pt/Al2O3: An In Situ X-ray Absorption Study, *ChemPhysChem*, 2017, **18**(2), 238–244.

37 J. Chen, K. Giewont, E. A. Walker, J. Lee, Y. Niu and E. A. Kyriakidou, Cobalt-Induced PdO Formation in Low-Loading Pd/BEA Catalysts for CH4 Oxidation, *ACS Catal.*, 2021, **11**(21), 13066–13076.

38 C.-H. Liu, J. Chen, T. J. Toops, J.-S. Choi, C. Thomas, M. J. Lance and E. A. Kyriakidou, Hydrothermally stable Pd/$SiO_2$@Zr Core@Shell catalysts for diesel oxidation applications, *Chem. Eng. J.*, 2021, 130637.

39 R. Oktavian, V. Amidelsi, A. Rasmito and G. Wibawa, Vapor pressure measurements of ethanol–isooctane and 1-butanol–isooctane systems using a new ebulliometer, *Fuel*, 2013, **107**, 47–51.

40 K. S. Sing, Reporting physisorption data for gas/solid systems with special reference to the determination of surface area and porosity (Recommendations 1984), *Pure Appl. Chem.*, 1985, **57**(4), 603–619.

41 J. Xu, M. Li, J. Qiu, X.-F. Zhang, Y. Feng and J. Yao, PEGylated deep eutectic solvent-assisted synthesis of CdS@$CeO_2$ composites with enhanced visible light photocatalytic ability, *Chem. Eng. J.*, 2020, **383**, 123135.

42 R. Zhang, H. Liu and D. He, Pure monoclinic ZrO2 prepared by hydrothermal method for isosynthesis, *Catal. Commun.*, 2012, **26**, 244–247.

43 M. R. Loghman-Estark, R. S. Razavi and H. Edris, Synthesis and thermal stability of nontransformable tetragonal (ZrO2) 0.96 (REO1. 5) 0.04 (RE= Sc3+, Y3+) nanocrystals, in *Defect and Diffusion Forum*, Trans Tech Publ, 2013, vol. 334, pp. 60–64.

44 Q. Yang, L. Li, X. Wang and Y. Ma, Tunable metal-support interaction of Pt/$CeO_2$ catalyst via surfactant-assisted strategy: Insight into the total oxidation of CO and toluene, *J. Hazard. Mater.*, 2022, **424**, 127601.

45 W. Tan, H. Alsenani, S. Xie, Y. Cai, P. Xu, A. Liu, J. Ji, F. Gao, L. Dong and E. Chukwu, Tuning Single-atom $Pt_1$–$CeO_2$ Catalyst for Efficient CO and $C_3H_6$ Oxidation: Size Effect of Ceria on Pt Structural Evolution, *ChemNanoMat*, 2020, **6**(12), 1797–1805.

46 L. Nie, D. Mei, H. Xiong, B. Peng, Z. Ren, X. I. P. Hernandez, A. DeLaRiva, M. Wang, M. H. Engelhard and L. Kovarik, Activation of surface lattice oxygen in single-atom Pt/CeO2 for low-temperature CO oxidation, *Science*, 2017, **358**(6369), 1419–1423.

47 W. Ruettinger, X. Liu, X. Xu and R. J. Farrauto, Effect of Mo and Re Promoters on the Activity and Stability of a Pt/$ZrO_2$ Water-Gas Shift Catalyst (Part 1), *Top. Catal.*, 2008, **51**(1–4), 60–67.

48 A. Litke, H. Frei, E. J. Hensen and J. P. Hofmann, Interfacial charge transfer in Pt-loaded $TiO_2$ P25 photocatalysts studied by in-situ diffuse reflectance FTIR spectroscopy of adsorbed CO, *J. Photochem. Photobiol., A*, 2019, **370**, 84–88.

49 K. Reed, A. Cormack, A. Kulkarni, M. Mayton, D. Sayle, F. Klaessig and B. Stadler, Exploring the properties and applications of nanoceria: is there still plenty of room at the bottom?, *Environ. Sci.: Nano*, 2014, **1**(5), 390–405.

50 V. Nicolini, E. Gambuzzi, G. Malavasi, L. Menabue, M. C. Menziani, G. Lusvardi, A. Pedone, F. Benedetti, P. Luches and S. D'Addato, Evidence of catalase mimetic activity in Ce3+/Ce4+ doped bioactive glasses, *J. Phys. Chem. B*, 2015, **119**(10), 4009–4019.

 